Cell Reports
Physical Science

CellPress
OPEN ACCESS

Article

Correlating lithium-ion transport and interfacial lithium microstructure evolution in solid-state batteries during the first cycle

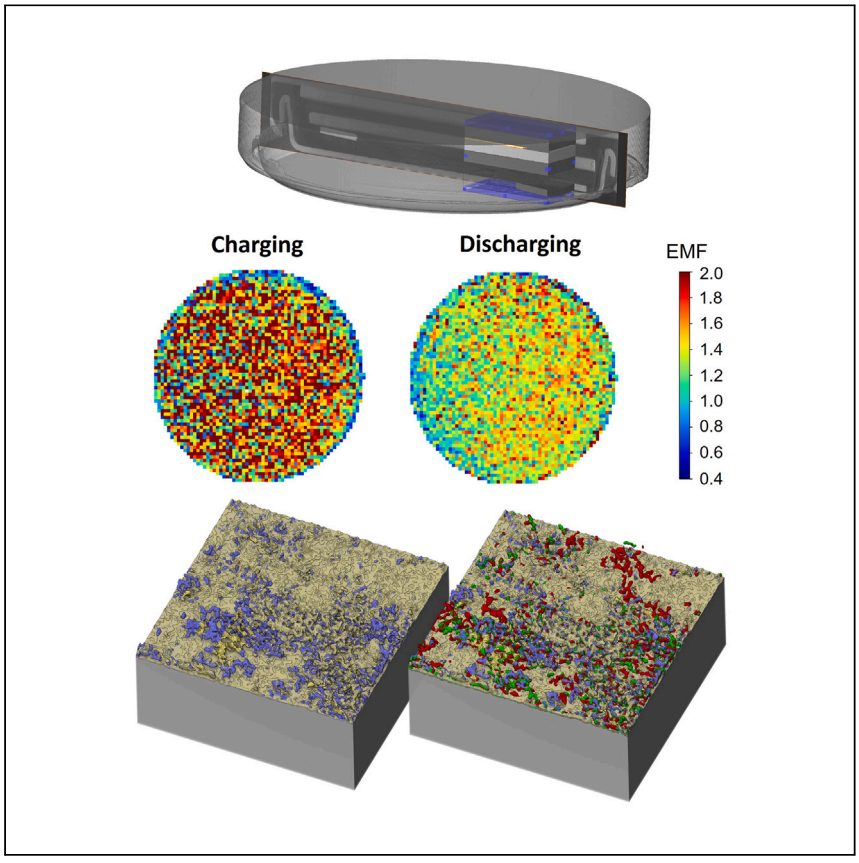

Huang et al. report an *operando* correlative X-ray Compton scattering and computed tomography imaging technique that correlates Li^+ concentration changes with Li morphology changes at the buried metal anode/solid polymer electrolyte interphase inside solid-state batteries. The study indicates that the stripping step forms irregular interfacial lithium morphologies at the expense of bulk anode volume shrinkage during the first cycle.

Chun Huang, Matthew D. Wilson, Ben Cline, ..., Matthieu N. Boone, Thomas Connolley, Chu Lun Alex Leung

a.huang@imperial.ac.uk

Highlights

Operando correlative X-ray Compton scattering-computed tomography (XCS-CT)

XCS-CT is used to distinguish Li^+ and Li^0 changes in solid-state Li-metal batteries

XCS maps Li^+-ion concentrations of cathode, anode, solid polymer electrolyte

CT reveals Li^0 morphology at buried anode/SSE interphase inside full cell

Huang et al., Cell Reports Physical Science 5, 101995
June 19, 2024
https://doi.org/10.1016/j.xcrp.2024.101995

Cell Reports
Physical Science

CellPress
OPEN ACCESS

Article

Correlating lithium-ion transport and interfacial lithium microstructure evolution in solid-state batteries during the first cycle

Chun Huang,[1,2,3,8,*] Matthew D. Wilson,[4] Ben Cline,[4] Abeiram Sivarajah,[1] Wiebe Stolp,[5] Matthieu N. Boone,[5] Thomas Connolley,[6] and Chu Lun Alex Leung[3,7]

SUMMARY

The formation of heterogeneous Li structures at the anode/solid polymer electrolyte (SPE) membrane interphase of solid-state Li-metal batteries (SSLMBs) is one of the key factors that impede SSLMB performance. The relationship between Li^+-ion transport kinetics and Li^0 structural evolution at the buried interphase is critical but challenging to characterize. Here, we report an *operando* correlative X-ray Compton scattering and computed tomography imaging technique that quantifies the changes of Li^+-ion concentrations in the bulk cathode, SPE membrane, and anode of the SSLMB full cell using a commercially standard configuration. We then visualize Li^+-ion concentration distributions as well as Li^0 microstructures at the buried anode/SPE interphase. Mechanistic analyses show that the Li-stripping step forms more irregular interfacial Li morphologies at the expense of bulk anode volume shrinkage compared to the Li-plating step during the first cycle.

INTRODUCTION

Solid-state Li-metal batteries (SSLMBs) are potentially safer to use because they use non-flammable solid-state electrolytes (SSEs), ceramic electrolytes,[1] or solid polymer electrolytes (SPEs) to replace conventional flammable liquid electrolytes. SSLMBs also significantly increase the theoretical energy density (~500 Wh kg^{-1}) due to the use of Li-metal anode compared with conventional Li-ion batteries with a graphite anode (~300 Wh kg^{-1}).[2] SPEs have the advantage of facile processing for large-scale production. During charging, Li^+ ions are extracted from the cathode, subsequently reduced, and deposited as Li^0 on the anode surface, i.e., Li plating. The Li^+-ion transport process is reversed during discharging, i.e., Li stripping. However, Li-metal anode exhibits large volume changes during charging and discharging and grows Li dendrites, which impede the SSLMB performance. This may lead to short circuit and causes safety hazards.

Several characterization techniques have been used for imaging Li morphological changes in SSLMBs. For example, focused ion beam scanning electron microscopy (SEM) and energy-dispersive spectrometry investigated Li dendrites on a $LiBH_4$ SSE after 50 cycles, showing Li dendrites in the grain boundary and pores of the SSEs.[3] A microprobe was coupled with *operando* SEM to observe the Li intrusion events through $Li_7La_3Zr_2O_{12}$ (LLZO) SSE.[4] *Operando* optical interferometric scattering microscopy has been used to observe nanoscopic Li^+-ion dynamics inside individual particles of cathode material Li_xCoO_2[5] and anode material $Nb_{14}W_3O_{44}$.[6] An atomic force microscopy cantilever was coupled with environmental transmission electron

[1]Department of Materials, Imperial College London, London SW7 2AZ, UK

[2]The Faraday Institution, Didcot OX11 0RA, UK

[3]Research Complex at Harwell, Rutherford Appleton Laboratory, Didcot OX11 0FA, UK

[4]STFC-UKRI, Rutherford Appleton Laboratory, Didcot OX11 0QX, UK

[5]Radiation Physics, Department of Physics and Astronomy, Ghent University, Proeftuinstraat 86/N12, 9000 Gent, Belgium

[6]Diamond Light Source, Didcot OX11 0QX, UK

[7]Department of Mechanical Engineering, University College London, London WC1E 7JE, UK

[8]Lead contact

*Correspondence: a.huang@imperial.ac.uk

https://doi.org/10.1016/j.xcrp.2024.101995

microscopy (TEM) to study the growth of a Li whisker under elastic constraint.[7] However, Li has high sensitivity to electron beams. The aforementioned methods cannot observe Li at the buried interphase inside an SSLMB cell, and TEM and optical imaging techniques usually have a relatively small field of view of one to a few particles. While observing the behavior of one to a few particles is critical for the study of underlying mechanisms, it is also important in studying the behavior at the interphase or at the cell level.

X-ray computed tomography (XCT)[8,9] and radiography[10] reveal battery internal microstructures; for example, *operando* XCT has been used to image the crack growth through a Li_6PS_5Cl SSE, concluding that Li initiation and propagation are two separate processes during Li plating.[9] Nano-XCT can achieve nanometer-scale resolutions, but the field of view is usually sacrificed, e.g., a spatial resolution of 50 nm with ~15 × ~15 μm^2 field of view.[11] Spectroscopy-based techniques can identify oxidation states and compositions of elements, e.g., X-ray near-edge absorption spectroscopy, usually used for investigating the chemical properties of heavy elements such as transition metals instead of Li, which is one of the lightest elements, as these heavy elements are more likely to exhibit characteristic edges or peaks due to the K, L, and M electron shells compared with Li (only K shell and L shell).[12,13] X-ray diffraction (XRD) and X-ray fluorescence (XRF)[14] have been combined to measure Li^+ intercalation into the electrodes (using XRD) and Li^+ concentration in the liquid electrolyte (using XRF),[15] but Li^+ does not present a fluorescence signal, so the experiment probed the As signal from a bespoke $LiAsF_6$ salt in the liquid electrolyte instead. The combination of XRD and XCT (i.e., XRD-CT) has recently attracted much attention for monitoring area-specific changes of phase and lattice parameters in electrodes[16] and current collectors,[17] but it is challenging for XRD to measure the subtle changes in lattice parameters after Li^+ insertion for amorphous materials, e.g., SPE.

Neutron radiography is more sensitive to Li element and isotopes,[18] but low natural abundances of ^6Li can lead to lower temporal resolutions than X-ray radiography.[19,20] Neutron depth profile (NDP) has been used to measure the Li-element concentration profiles in cells with different SSEs (LiPON, $Li_7La_3Zr_2O_{12}$ [LLZO], and Li_3PS_4) during Li plating,[21] but bespoke cell configurations were used for NDP. Nuclear magnetic resonance (NMR) can identify light elements and has been a valuable tool to study the fundamental Li mechanisms,[22,23] but usually bespoke cell configurations are used.[24] Overall, it is extremely challenging to distinguish, quantify, and visualize Li^+ and Li^0 in a full battery cell using commercially standard stainless-steel casings and using X-rays *in operando*. The difference in Li^+-ion transport kinetics between the plating and stripping steps during the first cycle and the origin of heterogeneous Li^0 morphology formation at the buried anode/SPE interphase remain unclear.[25]

Here, we use a new *operando* correlative X-ray Compton scattering (XCS) and XCT (i.e., XCS-CT) imaging method to firstly spatially resolve Li^+-ion concentration changes of the bulk cathode, SPE membrane, and anode inside an SSLMB full cell in a commercial coin-cell configuration with commercially standard stainless-steel casings over a large field of view (7 mm × 8 mm) during charging and discharging for the first time. We then focus on the buried anode/SPE interphase region (~65 μm in thickness) and correlate the Li^+-ion concentration changes and distributions with Li^0 microstructural evolution inside the cell. Compton scattering (X-ray inelastic, incoherent scattering) has been generally neglected in scattering experiments because the generated incoherent radiation does not give rise to the

interference effects that can only arise from coherently scattered photons.[26] Here, we show a new approach of using XCS to analyze Li^+-ion concentrations and correlating that with Li^0 microstructural evolution within a single experiment. We are also able to show the changes of both the Li anode bulk volume and the interfacial morphology at the cell level. The stripping step led to more irregular Li^0 morphology structure formation than that in the plating step during the first cycle.

RESULTS AND DISCUSSION

Operando XCS-CT of SSLMB

The SSLMB contained a Li anode, polyethylene oxide (PEO) SPE membrane with $LiC_2F_6NO_4S_2$ (LiTFSI) salt, and a $LiNi_{0.6}Mn_{0.2}Co_{0.2}O_2$ (NMC622)-based composite cathode mixed with the same SPE material. PEO offers attractive advantages such as good processability into relatively thin films (30 μm) at large scale.[27,28] The Li salt is dissolved in PEO by ion dissociation, while the Li^+ ions are complexed by the coordination of ethylene oxide (EO) groups in the polymer chain and are shuttled through the polymer matrix by rearrangement of the EO groups.[29] The SSLMB samples were assembled into a commercially standard CR2032 coin-cell configuration. A standard stainless-steel spring was used in the coin cell to homogenize the lateral pressure exerted onto the electrodes and the SPE membrane (optimal internal pressure was previously estimated to be 70–80 kPa[30]); no external pressure was applied to these coin cells.

Figure S1 is a photo of the experimental setup of the *operando* XCS-CT. High-energy (115 keV) monochromatic synchrotron X-rays were used to penetrate the stainless-steel battery casing for obtaining extended horizontal-field-of-view XCT images with off-centered samples to capture the entire cell with a spatial resolution of 3.24 × 3.24 μm^2 per pixel.[31,32] Each tomogram was captured by a scientific complementary metal-oxide-semiconductor (sCMOS) camera coupled with an optical module placed behind the battery. Figure 1A is a 3D volume rendering of the XCT images showing the coin cell and its internal components with a magnified view of the positions of the cathode and SPE membrane. Figure 1B is a 2D XCT reconstructed image along the x-z plane showing good adhesion of the SPE membrane onto the Li-metal surface and cathode surface throughout the x-y plane inside the cell at the pristine state.

The incident X-ray beam was then adjusted to a light sheet with a beam size of 25 × 0.25 mm^2 using beam-defining slits for XCS imaging of the battery[33] (shown schematically in Figure 1C). A 2D high-energy X-ray imaging technology (HEXITEC) CdZnTe detector[34,35] was placed at 90° to the incident X-rays above the battery cell and collected the X-ray scattering signals across the entire x-y plane of the battery. The HEXITEC detector had 80 × 80 pixels on a 0.25-mm pitch and was able to collect one XCS energy spectrum per pixel of all pixels across the x-y plane in a single shot to obtain region-specific XCS energy spectra, i.e., XCS imaging (for more details, see experimental procedures).

We then moved the SSLMB vertically to perform XCS imaging in three regions—(1) cathode-dominant, (2) interphase-dominant, and (3) Li-anode (just below the SPE membrane) regions—to capture XCS imaging at three different vertical regions of the SSLMB (magnified regions in Figure 1D). It is usually challenging to obtain the scattering signals from a region-specific component such as the SPE membrane and cathode, since the thicknesses of the SPE membrane (30 μm) and cathode (65 μm) were lower than the gap of the beam-defining slits (250 μm). Here, we

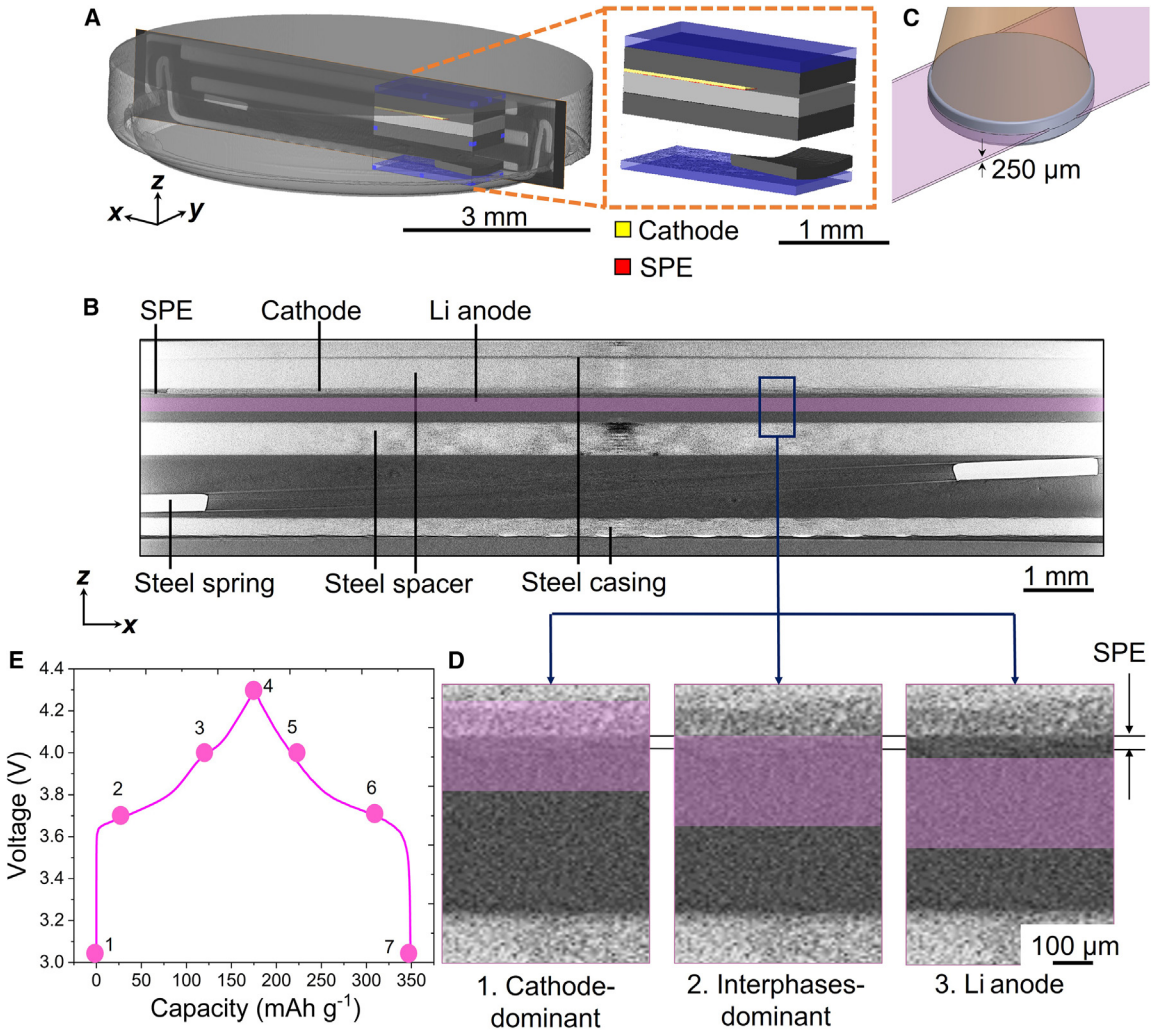

Figure 1. XCS-CT of SSLMB

(A) 3D volume rendering of X-ray computed tomography (XCT) reconstructed solid-state Li-metal battery (SSLMB) and its internal components in a commercially standard stainless-steel coin-cell casing. The red and yellow regions from the magnified figure are the cathode and solid polymer electrolyte (SPE) membrane, respectively, showing their positions inside the cell. Scale bar, 3 mm (inset, 1 mm).

(B) The reconstructed XCT x-z slice of the SSLMB cell showing that the components adhered to each other uniformly at the pristine state of SSLMB. Scale bar, 1 mm.

(C) Schematic of the coin cell and X-ray sheet beam for *operando* X-ray Compton scattering (XCS) imaging.

(D) Zoomed-in regions of the reconstructed XCT x-z slice of the SSLMB cell showing the three different vertical heights of the SSLMB being probed by XCS imaging. Scale bar, 100 μm.

(E) Galvanostatic charge and discharge profile of the SSLMB where XCS imaging was carried out during the states of (1) pristine (0% state of charge [SoC]), (2) charging I (20% SoC), (3) charging II (71% SoC), (4) fully charged (100% SoC), (5) discharging I (22% depth of discharge [DoD]), (6) discharging II (77% DoD), and (7) fully discharged (100% DoD); XCT imaging was carried out during the states of pristine, after charging I, fully charged, after discharging I, and fully discharged in a continuous process.

developed an analysis method of post-processing the overlapping XCS energy spectra to obtain the signals from the individual components (SPE membrane- and cathode-only, as detailed in experimental procedures). The SSLMB cell was continuously charged and discharged at a constant slow rate of 0.3 mA cm^{-2} (0.07 C based on the capacity of NMC622[36]) at the first cycle at room temperature during the XCS-CT experiment. The dots in the charge and discharge profile (Figure 1E) indicate the different states of charge (SoCs) and depths of discharge (DoDs) where the XCS imaging and XCT scans were obtained.

Electrochemical properties of SSLMB

Figures 2A and 2B, show an electrochemical impedance spectroscopy (EIS) plot of the SSLMB at different SoCs and DoDs in the first (dis)charge cycle at room temperature. The same configuration (cathode vs. Li-metal anode using a polymer electrolyte) has been used previously for studying SSLMBs with polymer electrolytes.[37–39] The intercept of the EIS plot and the *Re.Z′* axis is the series resistance R_s that represents resistance to electronic and ionic motion in the electrodes and SPE.[40] The impedance consists of a semicircle that represents charge transfer resistance R_{ct} in the electrodes and at the electrode/SPE interphase, similar to R_{ct} in other electrochemical systems using SPE[41]; this is followed by a Warburg response.[40] R_{ct} decreased during charging from 3.0 to 4.3 V and then increased during discharging from 4.3 to 3.0 V. R_s and R_{ct} values were measured >20 times from the EIS plots, and their corresponding uncertainties of R_s and R_{ct} were calculated to be $\pm$1% and $\pm$5%, respectively. Figure S2 is the EIS plot of the same battery at different SoCs and DoDs in the second (dis)charge cycle. Although R_{ct} decreased during charging and increased during discharging, the changes were smaller in the second cycle. This can be because Li plating took place on a pristine Li-metal surface with the smallest number of defects during first charging. A heterogeneous interfacial surface had been formed after the first plating, which led to more defects and more restricted Li^+-ion diffusion at the microscale during the first stripping.[42] The microstructure heterogeneity influences Li^+-ion diffusion kinetics at the microscale through defects such as nano- and micropores and cracks.[43–45] Three-electrode cells with Li-metal electrode vs. reference electrode impedance may shed light on the impedance changes of Li-metal anode upon plating and stripping. Three-electrode cells for liquid electrolyte batteries typically use a thin wire located within the wetted separator between the anode and cathode, but introducing a third electrode in solid-state batteries is complicated because the components are solid state and compacted together.[46–48] Nevertheless, using a specially engineered three-electrode cell for solid-state batteries,[46] the EIS data also led to the conclusion that an increase in impedance in the kHz frequency loop range upon stripping is associated with an increasing amount of porosity at the Li/electrolyte interphase,[46] which agrees with our XCS-CT data (shown below).

The *ex situ* galvanostatic (dis)charge profiles of the SSLMB at increasing (dis)charge rates (Figure S3) and its rate capability (Figure S4) show discharge capacities of 170.3 mAh g^{-1} (3.29 mAh cm^{-2}, 505.8 mAh cm^{-3}) and 134.2 mAh g^{-1} (2.59 mAh cm^{-2}, 398.6 mAh cm^{-3}) at 0.07 and 1 C, respectively, at 60°C following testing protocols similar to those in the literature; for example,[49] the ohmic drop from the (dis)charge profiles was 10, 30, 70, and 140 mV at 0.07, 0.2, 0.5, and 1 C, respectively. Figure S5 is a cyclic voltammogram of the stainless-steel/SPE/stainless-steel cell at a low scan rate of 0.1 mV s^{-1} at 60°C, showing the current was negligible at 0–4.4 V, and there was a small increase to 0.33 μA cm^{-2} at 4.4 V (magnified in the inset of Figure S5). This may be because the PEO-based SPE decomposed at higher voltages,[50–52] hence the galvanostatic (dis)charge voltage in Figure S3 was limited up to 4.3 V. Literature also reports that PEO can be slowly oxidized above 3.8 V at longer cycles, e.g., $\geq$10 cycles.[53] Here, we focus on the first cycle. The SSLMB achieved reversible capacity retention of 90% after 200 cycles at 60°C within the 3–4.3 V potential window (Figure S6), similar to other SSLMB studies.[54] Other than possible PEO decomposition at higher voltages, the capacity decrease may also be due to several other factors, e.g., cathode material, solid electrolyte interphase (SEI) on the anode, and cathode electrolyte interphase on the cathode.

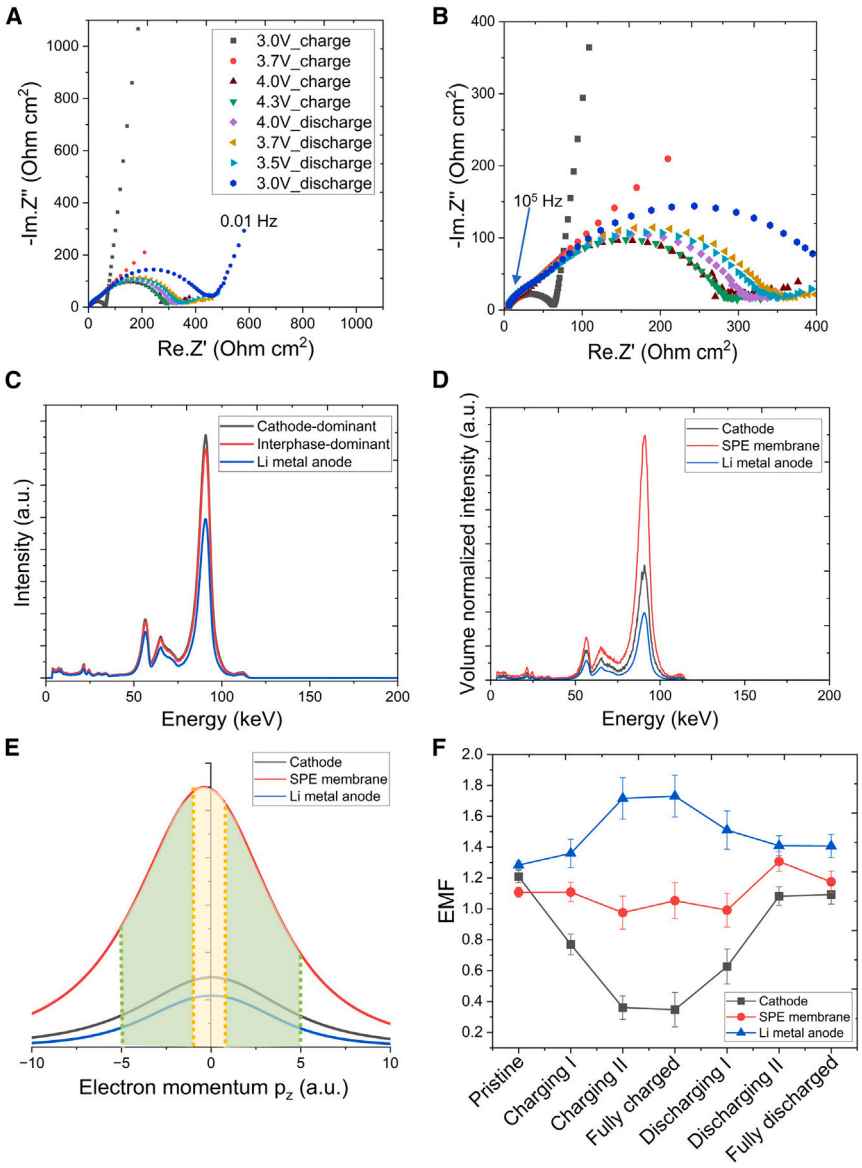

Figure 2. Electrochemical properties and Li^+-ion concentration of components inside SSLMB

(A and B) (A) Nyquist plot of the SSLMB at different SoCs and DoDs during the first (dis)charge cycle, and (B) a magnified high-frequency region of the Nyquist plot from (A).

(C) XCS energy spectra of the SSLMB at three probed regions at the charging I state (and other [dis] charging states in Figures S7–S12). The intensity of each energy spectrum is the sum of spatial data points of all pixels along the same x-y plane of the SSLMB.

(D) Normalized X-ray energy spectra of three individual components, cathode, SPE membrane, and anode, at the charging I state (and at other [dis]charging states in Figures S14–S19).

(E) Compton profiles of the cathode, SPE membrane, and anode at the charging I state (and other [dis]charging states in Figures S20–S25). The yellow region indicates low electron momentum and refers to the valence electrons, while the green region indicates high electron momentum and refers to the core electrons.

(F) Summary of electron momentum factor (EMF), the ratio between the low and high electron momentum densities, of the cathode, SPE membrane, and anode inside the SSLMB at all SoCs and DoDs during the first cycle. The error bars indicate the calculation uncertainties of EMF from the Compton profile.

Spatially resolved Li^+-ion concentrations in each component of SSLMB during (dis)charging

Figure 2C shows the X-ray scattering energy spectra from the three probed regions of the SSLMB. The lower energy peaks ($\leq$85 keV) are the associated XRF signals of Cd (22.9 and 26.1 keV) and Te (27.2 and 31.0 keV) from the HEXITEC detector, and XRF signals of W, Pb, and escape peaks (50–85 keV) from the pinhole shielding of the detector and when annihilation photons leave the detector.[35,55] The dominant peak at 93.9 keV is the Compton peak with a peak shift of 21.1 keV from the incident photons. The Compton peak intensity is directly proportional to the total electron density from each probed region (see Equation 1 in experimental procedures).[56,57] Figure 1D shows that the Li anode accounts for 89% volume in region 2. Since the number of Li atoms is directly proportional to the anode volume,[58] the signal intensities from the separator region are calculated from the intensities in region 2 minus 89% of the intensities in region 3. Similarly, region 1 accounts for 64% of the intensities in region 3 and the entire separator region. The intensities of the three components were then normalized by their individual volumes (for the detailed calculation method, see supplemental information). This method allows obtaining the XCS results with an improved spatial resolution along the z axis smaller than the beam size. We further compared the Compton profiles for the Li anode in region 3 from both the SSLMB and a Li-ion battery containing the same electrode materials and casing except that we used a conventional liquid electrolyte. Figure S13 shows the energy spectra of the two types of batteries in region 3 (the Li-metal anode region) where the energy spectra overlapped with each other, confirming that the signals from the anode region when the X-ray sheet beam was positioned at region 3 were not affected by the other materials from regions 1 and 2. This shows that the X-ray absorption at the extremely high incident X-ray energy of 115 keV was <1%,[59,60] hence validating the method of deducting the XCS signals from one region, e.g., the anode, to obtain the XCS signals from the other region, e.g., the separator, using the high incident X-ray energy.

Figure 2D shows the resulting volume normalized X-ray scattering energy spectra of the three specific components of SSLMB, namely (1) cathode, (2) SPE membrane, and (3) Li anode, after deducting the signals from the other components and normalized by the volume of each component, so that the peak intensities of each specific component can be compared to one another. The SPE membrane exhibited the most prominent Compton peak, indicating that the SPE membrane had the highest electron density among all the components, perhaps because (1) the SPE membrane was $\geq$98% dense in weight density and had a relatively high density ($\sim$1.7 g cm^{-3} vs. 0.5 g cm^{-3} for the Li-metal anode)[61] and (2) the high molecular weight of PEO (1,000,000 g mol^{-1}) formed a supramolecular structure where the long macromolecular chains contributed to a large number of free electrons. The cathode exhibited the second-highest Compton peak intensity. This may be because some of the pores in the cathode may not have been completely filled by PEO-LiTFSI. Optimization of the composite cathode density will be carried out in future studies. The energy spectra in Figures S14–S19 show that the difference between the different SoCs and DoDs for each component was small, as expected, because the proportion of electron number changes due to the Li^+-ion insertion and removal out of the total electron number per atom/molecule is low (e.g., 6.5% for NMC622). Compared with XCS-CT (shown below), most existing X-ray scattering methods only analyze the total number of electrons[12,16,17,62–64]; hence, they are insensitive to the subtle changes of Li^+-ion concentrations.

Figure 2E displays the Compton profile as a function of electron momentum p_z calculated from the Compton peak in Figure 2D using Equation 2 [65] for the cathode,

SPE membrane, and Li anode. The electron momentum is proportional to the electron orbital motion speed v; the Compton profile is sensitive to the different electron orbital motion speed (valence electrons $v = 1.8 \times 10^6$ m s^{-1}, core electrons $v = 2.2 \times 10^6$ m s^{-1}) and differentiates the valence and core electrons.[56] In the cathode, the valence electrons are transferred from the Li atoms to the electron orbital of the cathode material during redox reactions. The low electron momentum in the range of $-1 < p_z < 1$ refers to the valence electrons (yellow region in Figure 2E), whereas the high magnitude of electron momentum in the ranges of $-5 < p_z < -1$ and $1 < p_z < 5$ refers to the core electrons (green region), estimated by measuring the XCS energy spectra of the cathode only at the fully charged and discharged states,[66] which was performed on the cathode material with a liquid electrolyte to shed light on the electron momentum of the valence and core electrons of the electrode materials. The ratio of the areas under the Compton profile between the low and high electron momentum is the electron momentum factor (EMF, calculated using Equations 3, 4, and 5).Our previous results showed that the EMF increases linearly with the Li^+-ion concentration, x, in the cathode of $Li_xNi_{0.8}Mn_{0.1}Co_{0.1}O_2$ only, a relationship verified by measuring the Li concentration in the $Li_xNi_{0.8}Mn_{0.1}Co_{0.1}O_2$ compound using inductively coupled plasma optical emission spectrometry (ICP-OES).[31,33] Hence, EMF is able to amplify the signals of valence electrons and quantify the Li^+-ion concentration of the electrodes and SPE materials, where the light element Li signals are otherwise buried by the stronger signals from heavy elements when using conventional X-ray scattering techniques. The EMF shows the chemical composition change of the material; since the Li oxidation number is +1, one Li^+ and one electron are involved in each redox chemical reaction,[67] whereas at the crystallographic level, there can be more than two Li^+ ions moving together to vacant sites.[68]

Figure 2F summarizes the changes of EMF, which reflects the changes of Li^+-ion concentration in each component of the SSLMB at different SoCs and DoDs of the first cycle. For example, the EMF of the anode increased during charging, indicating more incoming Li^+ ions onto the Li-metal anode surface. Meanwhile the EMF of the anode decreased during discharging, indicating the amount of Li^+ ions being removed from the Li-metal anode surface. The EMF of the cathode decreased rapidly by an absolute rate change of 93.5% from pristine to charging I and by an absolute rate change of 94% from charging I to charging II, reaching almost minimum at charging II; the voltage of the SSLMB was held from charging II to fully charged. Similarly, the EMF of the anode increased rapidly from pristine to almost maximum at charging II, showing that the SSLMB almost reached a fully charged state at charging II. The SEI formation was more rapid at the beginning of charging under fast kinetics prior to and at the beginning of the onset of the intercalation redox.[69] In contrast, the EMF of the cathode increased by an absolute rate change of 32.4% from fully charged to discharging I and by an absolute rate change of 78.3% from discharging I to discharging II, and the EMF of the anode decreased at a similar rate, showing that: (1) Li^+-ion transport kinetics of the two electrodes influence each other because Li^+ ions travel between the two electrodes during (dis)charging; and (2) Li^+-ion transport kinetics are faster during charging (Li plating) than discharging (Li stripping) at the first cycle. The asymmetric rate performance during lithiation and delithiation has been shown previously by either cathode or anode individually, e.g., silicon nanofilm anode.[70] Here, we show the correlation of the asymmetric Li^+-ion concentration-rate changes between the cathode and anode inside an SSLMB full cell with SPE during lithiation and delithiation *in operando*. The EMF of the SPE membrane fluctuated and increased slightly at discharging II and at the end of discharge, possibly due to

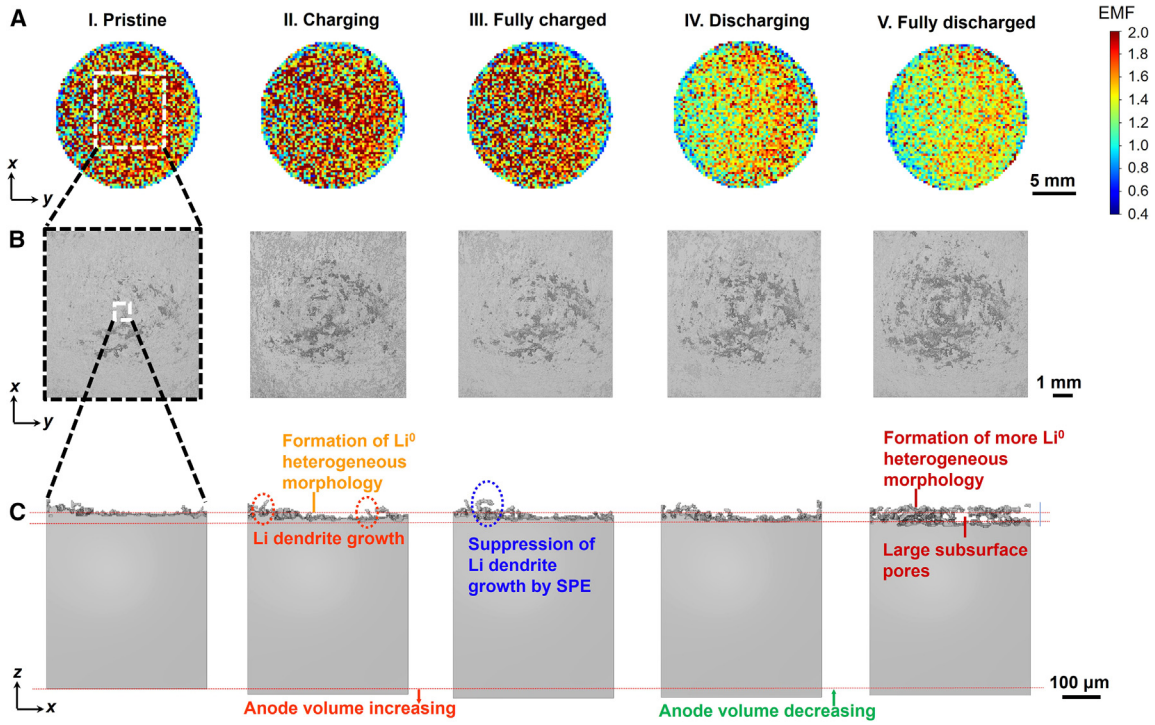

Figure 3. Correlative XCS-CT of buried anode/SPE interphase on the anode side inside SSLMB during different states of the first cycle

Imaging is shown at (I) pristine, (II) charging, (III) fully charged, (IV) discharging, and (V) fully discharged states of the first cycle.

(A) EMF mapping of Li^+-ion concentration distributions obtained by XCS imaging in the x-y plane. Scale bar, 5 mm.

(B) Reconstructed topological images of Li^0 morphology obtained by XCT in the x-y plane. Scale bar, 1 mm.

(C) Reconstructed images of Li^0 morphology obtained by XCT in the x-z plane, showing both the evolution of individual Li dendrite, porous structure, and formation of subsurface pores on the anode surface, and the Li anode bulk volume changes. Scale bar, 100 μm.

the detection of highly irregular Li^0 structure at the anode/SPE interphase (shown by XCT below).

Correlating Li^+-ion concentrations, Li^+-ion transport kinetics, and interfacial Li^0 microstructural evolution

Figure 3A shows EMF mapping of the buried anode/SPE interphase on the anode side along the x-y plane by XCS imaging at the different SoCs and DoDs of the first cycle with a spatial resolution of 250 × 250 μm^2 per pixel. The overall Li^+-ion concentration was higher during charging and decreased during discharging because Li^+ ions moved from the cathode to the anode/SPE interphase and into the anode during charging, and Li^+ ions moved from the anode to the anode/SPE interphase and then into the cathode during discharging, and this interphase was the surface of the Li anode with a portion of the bulk Li anode underneath. The changes in EMF also indicate the possibility of contribution from the formation of SEI at the anode interphase as PEO reduces after being in contact with Li metal.[71] The Li^+-ion concentrations were laterally heterogeneous with a higher Li^+-ion concentration in the middle of the anode than around the circular edge of the electrode, because the area of the anode (diameter = 16 mm) was higher than that of the cathode (diameter = 14 cm) according to the conventional method of coin-cell assembly that maximizes the available capacity.[72] Interestingly, the XCS-CT method was able to detect the middle "overlapped" area on the anode that exhibited a higher utilization efficiency in the electrochemical reaction of Li^+-ion exchange, showing the sensitivity of the technique. The XCS imaging results show that the majority of the interphase had

high Li^+-ion concentrations at charging (stage II) and fully charged (stage III), whereas the left half of the interphase exhibited low Li^+ concentrations and the right half of the interphase exhibited higher Li^+ concentrations at discharging (stage IV) and fully discharged (stage V), showing a higher level of heterogeneity in Li^+-ion concentration distributions during discharging (Li stripping) than during charging (Li plating) at the first cycle.

Figure 3B shows a series of zoomed-in XCT reconstructed images in the x-y plane in the middle region of the interphase with a spatial resolution of 3.24 × 3.24 μm^2 per pixel. XCT detects the change of X-ray attenuation where the attenuation change is due to formation of a new solid (Li^0). XCT has a higher spatial resolution than XCS imaging because XCT is based on the difference in X-ray attenuation of different materials[11] whereas obtaining a full energy spectrum per pixel is a requirement for XCS EMF mapping. The dark-gray region at the pristine state (stage I) indicates surface defects, e.g., slip lines or scratches,[73] on the commercial Li foil, which have possibly arisen during Li foil forming and/or handling processes. The XCT reconstructed images show that Li^0 first grew on the defect sites because the defect sites exhibit a low Gibbs free energy of Li^0 nucleation,[74] after which Li^0 started to grow on the relatively smooth anode surface during charging (II → III) and continued to grow during discharging (IV → V).

Figure 3C shows the further zoomed-in XCT 3D reconstructed images in the x-z plane to visualize both the bulk Li-anode volume changes and the individual Li dendrites and subsurface porous structures at the anode/SPE interphase simultaneously. The images show that there was a slight unevenness on the commercial Li chip surface at the pristine state. The entire Li anode was pushed down by the SPE as the anode expanded (total volume of the anode increased by 3.7%), and Li dendrites and heterogeneous Li structures grew from pristine to fully charged (stage III). SEI formation may also be captured along with Li^0 dendrite formation. Li dendrites were observed to have grown sideways at stage III due to the suppression by the SPE. Previous measurements show that the shear modulus of PEO (>10^5 Pa[75]) exhibits a good Li-dendrite growth resistance. Here, we show the interactions between the Li-dendrite morphology changes and the PEO-based SPE membrane *in operando*. The Li-anode volume then contracted (total volume of the anode decreased by 1.4%) from fully charged (stage III) to fully discharged (stage IV) at the first cycle. One striking observation was that although the Li^+-ion concentration was lower and the anode bulk volume decreased, the Li morphology was more heterogeneous and there was a higher proportion of irregular Li^0 microstructure. This may be caused by the formation of more large subsurface pores at the interphase at first discharging than at first charging (shown in Figure 3C). To quantify the changes of surface roughness R_a across the large field of view at the anode/SPE interphase, the XCT volume was converted into a surface topological map in each (dis)charge state (Figure S26), R_a was calculated using Equation 6, and the root-mean-square deviation of roughness R_q was calculated using Equation 7; both are summarized in Table S1. R_a was 5.1, 5.4, and 6.1 ± 0.005 μm at the pristine, fully charged, and fully discharged states, respectively, i.e., R_a increased by 6% from pristine to fully charged and continued to increase by a faster rate of 13.5% from fully charged to fully discharged, while R_q showed the same trend. Table 1 summarizes the changes of EMF and R_a.

Figures 4A–4E show a series of 3D reconstructed XCT volumes that track the irregular Li^0 structure formation and evolution at the buried anode/SPE interphase, with one color for the morphology changes at each stage across the stages I–V. The 3D

Table 1. Summary of measured properties and their change rates across (dis)charging states

	Pristine	Fully charged (Li plating)	Fully discharged (Li stripping)	Difference between pristine and fully charged (%)	Difference between pristine and fully discharged (%)
EMF from XCS imaging (a.u.)	1.28	1.73	1.41	+35.2	+10.2
Surface roughness R_a from XCT (μm)	5.1	5.4	6.1	+5.9	+19.5

Changes in EMF of the anode at the buried anode/SPE interphase inside the SSLMB by XCS; and surface roughness R_a at the same interphase by XCT at different (dis)charge states of the first cycle.

volume rendering confirms that heterogeneous Li^0 morphology started to form at the interphase during charging, and the heterogeneous Li^0 morphology continued to grow more during discharging. Using finite element-based simulations (for method see Huang and Grant[76]), Figure S27 shows simulated Li^+-ion flux of the segmented XCT volume in the same region at the fully charged and discharged states to take into account the influence of the interfacial microstructure changes on Li^+-ion transport kinetics. The Li^+-ion transport flux decreased from fully charged to fully discharged at the first cycle as the interfacial microstructure became more irregular and subsurface porosity increased.

During the first plating step, a small portion of heterogeneous Li-dendritic structures were formed on the pristine Li-metal surface as demonstrated by the 2D XCT results along x-y and x-z planes in Figures 3B and 3C and by the 3D interfacial microstructural changes tracking from the XCT results in Figures 4A–4C. The formation of these Li-dendritic structures may cause more restricted Li^+-ion flux during the subsequent first stripping step. This corroborates with the simulated Li^+-ion flux results along the x-y plane at the Li-metal anode/SPE interphase, which is based on the microstructural features from the XCT at the end of first plating and at the end of first stripping in Figure S27.

The more restricted Li^+-ion flux during the first Li stripping led to: (1) an even more heterogeneous Li^+-ion concentration distribution at the Li-metal anode/SPE interphase during the first stripping (as shown by the XCS imaging results in Figure 3A); and (2) a higher interfacial roughness than Li plating in the x-z plane due to more irregular Li-dendritic growth and subsurface pore formation even though the bulk anode volume decreased during the first Li stripping (as shown by the quantification of surface roughness R_a from the XCT results in Table 1 and the XCT imaging results in Figures 3C, 4D, and 4E). Thus, both Li plating and Li stripping lead to the growth of heterogeneous Li features; however, the irregular Li^0 structures have a much faster growth rate during the first stripping step than during the first plating step even at a relatively low current density of 0.3 mA cm^{-2}, much lower than the critical current density of ~1 mA cm^{-2} for Li-dendrite formation during plating at a similar pressure as previously estimated.[77] Previous experiments showed that pouch cells achieved a higher capacity of 240 mAh with a faster charge rate of C/4 and a slower discharge rate of D/10 than a capacity of 234 mAh achieved by a slower charge of C/10 and a faster discharge of D/4 at the first cycle,[78] the reason for which was not understood. Our results explain the underlying mechanism for these asymmetric plating and stripping rates for SSLMBs with SPE at the first cycle.

In summary, this is the first study of *operando* XCS-CT visualization and measurement of the bulk cathode, SPE membrane, and anode of SSLMBs with a commercially standard stainless-steel casing that focuses on the buried anode/SPE

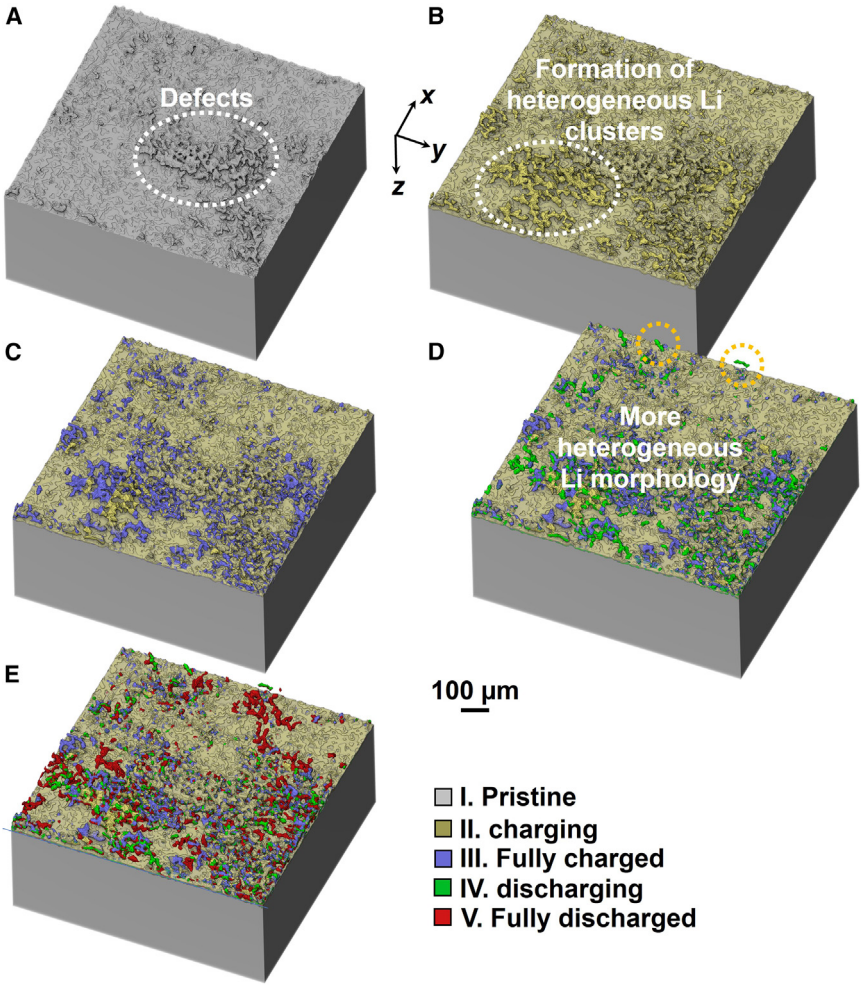

Figure 4. 3D Li morphology evolution

(A–E) 3D XCT volume rendering of the buried Li-metal anode/SPE interphase inside SSLMB at (I) pristine, (II) charging, (III) fully charged, (IV) discharging, and (V) fully discharged states of the first cycle, where color mapping (gray, yellow, dark blue, green, red) shows the Li morphology changes at each state. Scale bar, 100 µm.

interphase inside the operating SSLMB device. We correlate spatially resolved Li^+-ion concentration changes in the cathode, SPE membrane, and anode as well as Li^0 microstructural formation and evolution across the interphase at the first charging and discharging cycle. During the first discharging step, XCS imaging shows a slower absolute change rate of Li^+-ion concentration in both cathode and anode and a more heterogeneous Li^+-ion concentration distribution at the anode/SPE interphase. XCT 2D images and 3D volume rendering track and quantify the formation and growth of more heterogeneous Li^0 structures at the interphase at the expense of contraction of the Li bulk anode, and finite element-based computational simulations show more restricted Li^+-ion flux. Corroborating these results, we show that the origin of formation and growth of heterogeneous Li^0 structures and subsurface pores at the anode/SPE interphase is due to the slower Li^+-ion transport kinetics during the first Li stripping compared with the first Li plating on a pristine Li-metal surface. Our uncovered mechanism may inspire mixing different asymmetric charging and discharging protocols during the first cycle to achieve more homogeneous interfacial structures in real-life SSLMB applications. The proposed

mechanism can potentially benefit other metal anode batteries, e.g., Na, K, and Zn, to prevent excessive metal dendrites and moss-structure formation.

EXPERIMENTAL PROCEDURES

Resource availability

Lead contact

Further information and requests for resources and materials should be directed to and will be fulfilled by the lead contact, Chun Huang (a.huang@imperial.ac.uk).

Materials availability

This study did not generate new unique materials.

Data and code availability

The original data supporting the current study are available from the lead contact on request.

Fabrication and electrochemical testing

The SPE was a mixture of PEO and lithium bis(trifluoromethanesulfonyl)imide (LiTFSI) salt (Sigma-Aldrich) that was dissolved ([EO]/[Li^+] = 15:1) in acetonitrile (Sigma-Aldrich). The mixture was stirred at 60°C for 24 h to form a homogeneous solution. After casting the solution and evaporation of acetonitrile, the composite electrolyte was dried at 40°C for 24 h, the final SPE film was 30 μm in thickness and was cut into a circle shape of 18 mm in diameter. The molecular weight of the PEO was 1,000,000 g mol^{-1}, and the SPE had an ionic conductivity of 1.75×10^{-4} S cm^{-1} at 50°C. NMC622 powder was provided by Targray. A cathode slurry was prepared by homogeneously mixing the electrode active material NMC622, carbon electrical conductivity enhancer, and polyvinylidene fluoride (PVDF) binder at a weight ratio of 90:5:5 in *N*-methylpyrrolidine, stirred overnight, cast on an Al foil, and dried in vacuum at 80°C for 12 h. The PEO-LiTFSI solution was dropped onto the cathode disks to obtain composite cathodes after drying at 60°C for 12 h following a procedure described by Xiong et al.[79] The cathode, anode, and SPE were assembled into standard stainless-steel coin cells (CR2032) in an argon-filled glovebox. For comparison, Li-ion batteries using the same electrodes, standard liquid electrolyte of 1 M $LiPF_6$ dissolved in mixed solvents of ethylene carbonate and diethyl carbonate 1:1 (v/v), and a standard polypropylene-polyethylene-polypropylene separator were also assembled into the same CR2032 stainless-steel coin cells using the same procedure.

During the beamtime experiment, the cells were galvanostatically charged and discharged at a typical operating range of 3–4.3 V using a Gamry reference 600/EIS300 potentiostat/galvanostat at room temperature. Additional *ex situ* galvanostatic (dis)charge of SSLMBs was performed at various C rates of 0.07, 0.2, 0.5, and 1 C, and cycling stability tests were performed at 0.2 C and 60°C following similar testing protocols in the literature, e.g., Lu et al.[49] Cyclic voltammetry was performed by using a stainless-steel/SPE/stainless-steel coin-cell configuration at a scan rate of 0.1 mV s^{-1} at 60°C, whereby four cycles were performed in total. EIS of the full cells was conducted at 10^5–0.1 Hz with a 10-mV amplitude perturbation at different (dis)charging voltages in the first charge and discharge cycle at room temperature to reflect the impedance changes during the beamtime experiment.

Operando correlative XCS-CT

XCT imaging was conducted using a transmission geometry bent Laue double crystal monochromator with a highly coherent 115 keV X-ray beam. XCT and XCS

imaging were alternately used during battery (dis)charging. For the XCT scans, the incident X-ray beam had a size of 25 × 5 mm^2 to scan the entire battery, and a PCO.Edge 5.5 sCMOS camera coupled to a 100-μm-thick LYSO scintillator through a 0.82× magnification lens were used to collect the transmission images (Figure S1). The XCT scan consisted of 3,600 projections over 180° with an exposure time of 9 ms per projection.

For XCS imaging, the incident X-ray beam size was adjusted to 25 × 0.25 mm^2 using beam slits, where the x-y plane of the SSLMB cell was aligned to be parallel to the sheet beam, and spatially resolved X-ray scattering energy spectra were collected and recorded as a hyperspectral cube. The X-rays were collected perpendicular to the incident X-ray beam using a 2D HEXITEC CdZnTe detector.[34] Imaging was projected through a 0.2-mm pinhole in a 2-mm-thick W plate at 160 mm from the sheet beam, with the HEXITEC 2-mm-thick CdZnTe detector positioned a further 150 mm from the pinhole. Lead shielding of 10 mm thickness was used to shield the detector from the X-rays that were not originating from the sample. The temperature of the detector was maintained at 18°C with a bias voltage of −1,000 V applied. The detector consisted of an 80 × 80 pixels array on a 0.25-mm pitch, with a full energy-resolved X-ray spectrum measured for each pixel and all spectra captured simultaneously. The average energy resolution (full width at half maximum) of a pixel was measured to be 0.79 ± 0.15 keV using the 59.54 keV line from an Am-241 sealed source,[35] and the variation on peak energy due to the slight shift of the 90° position of the detector for the measuring scattering angle was measured to be ±2%. Calibration measurements were performed on a completely homogeneous disk. The detector was read out using SpecXiDAQ software, operating at a continuous frame rate of 9 kHz, with the energy and position of every individual X-ray photon output as raw data. The recorded data from the camera began when the data acquisition software received a trigger. Charge-sharing Compton X-ray interactions in the CdZnTe events that spanned more than two neighboring pixels were excluded from the spectral reconstructions. We further measured and compared the intensities of the Compton peaks from another Li-ion battery containing the same electrode materials, except for use of a liquid electrolyte, using the same XCS imaging setup.

Data processing for XCS-CT

The raw data were converted into a data cube with a dimension of 80 × 80 × (4.5 × 10^6) (pixel × pixel × number of frames) using software described by Van Assche et al.[55] Thereafter, the raw data cube underwent dark-field, offset, gain, and charge-sharing corrections. The resulting data cube was binned with an energy bin width of 0.2 keV. To perform correlative XCS-CT, we applied an XCT mask of either electrodes or SPE to its corresponding XCS spectrum per pixel fitted to the Compton peak around 93.9 keV. The angular distribution (cross-sections) of photons scattered from a single free electron is described by the Klein-Nishina formula. This formula gives the probability of scattering a photon into the solid angle element when the incident photon flux is φ_0. The intensity of the peak dN is related to the electron density of the material ρ_e excited by the X-ray radiation through Equation 1:

$$dN = \varphi_0 t_1 t_2 \rho_e dV \frac{d\sigma_{KN}}{d\Omega}, \qquad \text{(Equation 1)}$$

where t_1 is the incident X-ray transmittance from the entrance surface to the probing volume, t_2 is the scattered X-ray transmittance from the probing volume to the exit surface, dV is the probing volume, and $d\sigma_{KN}/d\Omega$ is the Klein-Nishina differential

cross-section. A Compton profile was generated at each pixel from the Compton scattering energy peak at 93.9 keV through Equation 2:

$$\frac{p_z}{mc} \cong \frac{E_2 - E_1 + \left(\frac{E_2 E_1}{mc^2}\right)\left(1 - \cos\theta\right)}{\sqrt{E_1^2 + E_2^2 - 2E_1 E_2 \cos\theta}}, \quad \text{(Equation 2)}$$

where p_z is a projection of the electron momentum in the core and valence orbitals of the atom or molecule, E_1 and E_2 are energies of the incident and Compton scattered X-rays, respectively, m is the electron mass, c is the speed of light, and θ is the scattering angle. The Li^+-ion concentration was estimated from the proportion of occupied valence electron orbitals among the core electron orbitals through the EMF according to Equation 3:

$$\mathrm{EMF} = \frac{E_L}{E_H}, \quad \text{(Equation 3)}$$

where E_L and E_H are the integral of low and high electron momentum densities in the electron momentum profiles, as shown by Equations 4 and 5:

$$E_L = \int_{-1}^{1} J(p_z)\,dp_z, \quad \text{(Equation 4)}$$

$$E_H = \int_{-5}^{-1} J(p_z)\,dp_z + \int_{1}^{5} J(p_z)\,dp_z. \quad \text{(Equation 5)}$$

Tomographic reconstruction was performed using SAVU and the ASTRA toolbox. We used a filtered back-projection and a ring artifact removing algorithms to the collected data. This was followed by 3D image processing, quantification, and data visualization using a combination of ImageJ, MATLAB 2019b (MathWorks, USA), and Avizo 2019.2 (Thermo Fisher Scientific, USA). We performed a 3D median filter with a kernel of 3 × 3 × 3, morphological opening with a radius of 3 voxels, auto-thresholding using factorization method, and connected component analysis to the components. Li^+ ions were simulated moving from one side of the buried SPE/anode interphase to the other in the x-y plane according to a difference in ion concentration imposed on opposite faces of the volume using TauFactor in MATLAB, as shown in previous studies.[28]

For calculating surface roughness changes of the buried lithium metal anode/SPE interphase inside the SSLMB during (dis)charging, the XCT volume was converted into a surface topological map at different (dis)charging states. The average surface roughness R_a provides the mean height of the magnitude of both protrusions and pitting vs. average plane, and was calculated using Equation 6:

$$R_a = \frac{1}{A}\iint |Z(x,y)|\,dxdy, \quad \text{(Equation 6)}$$

where $Z(x, y)$ is the absolute ordinate within the area of A, and there are a total of >6 million data points per calculation. The root-mean-square deviation of roughness R_q corresponds to the standard deviation of the height distributions and was calculated by Equation 7:

$$R_q = \sqrt{\frac{1}{A}\iint Z^2(x,y)\,dxdy}. \quad \text{(Equation 7)}$$

SUPPLEMENTAL INFORMATION

Supplemental information can be found online at https://doi.org/10.1016/j.xcrp.2024.101995.

ACKNOWLEDGMENTS

C.H. acknowledges the following funding: Faraday Institution Research grants FIRG060 and FIRG066; ERC Starting Grant, converted to UKRI funding EP/Y009908/1; UKRI EPSRC Innovation Fellowship EP/S001239/1 and EP/S001239/2; Faraday Institution Industry Fellowship FIIF015; Faraday Institution training grant FITG034; Imperial College London UKRI Impact Acceleration Account EP/X52556X/1; and Diamond Light Source beamtime MG29851-1. C.L.A.L. acknowledges the following funding: IPG Photonics/RAEng Senior Research Fellowship in SEARCH (ref: RCSRF2324-18-71); UKRI EPSRC Future Manufacturing Hub EP/P006566/1; UKRI EPSRC Manufacturing by Design EP/W003333/1; UKRI EPSRC Made Smarter Innovation - Materials Made Smarter Research Centre EP/V061798/1; UKRI EPSRC Data-driven, Reliable, and Effective Additive Manufacturing using Multi-BEAM technologies EP/W037483/1; and UKRI EPSRC Performance-Driven Design of Aluminium Alloys for Additive Manufacturing EP/W006774/1. W.S. acknowledges funding of the Research Foundation - Flanders (FWO) for the financial support (project 3G010820). We also acknowledge the use of facilities and support provided by the Research Complex at Harwell and JEEP-I12 beamline at Diamond Light Source, UK. Many thanks are extended to Dr. Enzo Liotti, Prof. Steve Collins, and Dr. Oxana Magdysyuk for participation in the beamtime experiment.

AUTHOR CONTRIBUTIONS

Conceptualization, C.H.; sample preparation, C.H.; *ex situ* characterization, C.H.; beamtime experiment investigation, C.H., M.D.W., B.C., A.S., W.S., T.C., and C.L.A.L.; data analysis, C.H., M.D.W., B.C., and C.L.A.L.; funding acquisition, C.H. and C.L.A.L.; writing—original draft, C.H. and C.L.A.L.; writing—review & editing, C.H., M.D.W., B.C., M.N.B., T.C., and C.L.A.L.

DECLARATION OF INTERESTS

The authors declare no competing interests.

Received: January 9, 2024
Revised: March 10, 2024
Accepted: April 30, 2024
Published: May 21, 2024

REFERENCES

1. Li, Y., Song, S., Kim, H., Nomoto, K., Kim, H., Sun, X., Hori, S., Suzuki, K., Matsui, N., Hirayama, M., et al. (2023). A lithium superionic conductor for millimeter-thick battery electrode. Science *381*, 50–53. https://doi.org/10.1126/science.add7138.

2. Zeng, Y., Ouyang, B., Liu, J., Byeon, Y.-W., Cai, Z., Miara, L.J., Wang, Y., and Ceder, G. (2022). High-entropy mechanism to boost ionic conductivity. Science *378*, 1320–1324.

3. Mo, F., Ruan, J., Sun, S., Lian, Z., Yang, S., Yue, X., Song, Y., Zhou, Y.N., Fang, F., Sun, G., et al. (2019). Inside or outside: origin of lithium dendrite formation of all solid-state electrolytes. Adv. Energy Mater. *9*, 1902123.

4. McConohy, G., Xu, X., Cui, T., Barks, E., Wang, S., Kaeli, E., Melamed, C., Gu, X.W., and Chueh, W.C. (2023). Mechanical regulation of lithium intrusion probability in garnet solid electrolytes. Nat. Energy *8*, 241–250.

5. Merryweather, A.J., Schnedermann, C., Jacquet, Q., Grey, C.P., and Rao, A. (2021). Operando optical tracking of single-particle ion dynamics in batteries. Nature *594*, 522–528.

6. Merryweather, A.J., Jacquet, Q., Emge, S.P., Schnedermann, C., Rao, A., and Grey, C.P. (2022). Operando monitoring of single-particle kinetic state-of-charge heterogeneities and cracking in high-rate Li-ion anodes. Nat. Mater. *21*, 1306–1313.

7. He, Y., Ren, X., Xu, Y., Engelhard, M.H., Li, X., Xiao, J., Liu, J., Zhang, J.-G., Xu, W., and Wang, C. (2019). Origin of lithium whisker formation and growth under stress. Nat. Nanotechnol. *14*, 1042–1047.

8. Ning, Z., Jolly, D.S., Li, G., De Meyere, R., Pu, S.D., Chen, Y., Kasemchainan, J., Ihli, J., Gong, C., Liu, B., et al. (2021). Visualizing plating-induced cracking in lithium-anode solid-electrolyte cells. Nat. Mater. *20*, 1121–1129.

9. Ning, Z., Li, G., Melvin, D.L.R., Chen, Y., Bu, J., Spencer-Jolly, D., Liu, J., Hu, B., Gao, X., Perera, J., et al. (2023). Dendrite initiation and propagation in lithium metal solid-state batteries. Nature *618*, 287–293.

10. Pfaff, J., Fransson, M., Broche, L., Buckwell, M., Finegan, D.P., Moser, S., Schopferer, S., Nau, S., Shearing, P.R., and Rack, A. (2023). In situ chamber for studying battery failure using high-speed synchrotron radiography. J. Synchrotron Radiat. *30*, 192–199.

11. Withers, P.J., Bouman, C., Carmignato, S., Cnudde, V., Grimaldi, D., Hagen, C.K., Maire, E., Manley, M., Du Plessis, A., and Stock, S.R. (2021). X-ray computed tomography. Nat. Rev. Methods Primers *1*, 18.

12. Heenan, T.M.M., Wade, A., Tan, C., Parker, J.E., Matras, D., Leach, A.S., Robinson, J.B., Llewellyn, A., Dimitrijevic, A., Jervis, R., et al. (2020). Identifying the origins of

microstructural defects such as cracking within Ni-rich NMC811 cathode particles for lithium-ion batteries. Adv. Energy Mater. *10*, 2002655.

13. Xu, Z., Wang, J., Guo, Z., Xie, F., Liu, H., Yadegari, H., Tebyetekerwa, M., Ryan, M.P., Hu, Y.S., and Titirici, M.M. (2022). The Role of Hydrothermal Carbonization in Sustainable Sodium-Ion Battery Anodes. Adv. Energy Mater. *12*, 2200208.

14. Quinn, P.D., Cacho-Nerin, F., Gomez-Gonzalez, M.A., Parker, J.E., Poon, T., and Walker, J.M. (2023). Differential phase contrast for quantitative imaging and spectro-microscopy at a nanoprobe beamline. J. Synchrotron Radiat. *30*, 200–207.

15. Dawkins, J.I., Martens, I., Danis, A., Beaulieu, I., Chhin, D., Mirolo, M., Drnec, J., Schougaard, S.B., and Mauzeroll, J. (2023). Mapping the total lithium inventory of Li-ion batteries. Joule *7*, 2783–2797.

16. Daemi, S.R., Tan, C., Vamvakeros, A., Heenan, T.M.M., Finegan, D.P., Di Michiel, M., Beale, A.M., Cookson, J., Petrucco, E., Weaving, J.S., et al. (2020). Exploring cycling induced crystallographic change in NMC with X-ray diffraction computed tomography. Phys. Chem. Chem. Phys. *22*, 17814–17823.

17. Heenan, T.M.M., Mombrini, I., Llewellyn, A., Checchia, S., Tan, C., Johnson, M.J., Jnawali, A., Garbarino, G., Jervis, R., Brett, D.J.L., et al. (2023). Mapping internal temperatures during high-rate battery applications. Nature *617*, 507–512.

18. Ziesche, R.F., Tremsin, A.S., Huang, C., Tan, C., Grant, P.S., Storm, M., Brett, D.J.L., Shearing, P.R., and Kockelmann, W. (2020). 4D Bragg edge tomography of directional ice templated graphite electrodes. J. Imaging *6*, 136.

19. Liu, D.X., Wang, J., Pan, K., Qiu, J., Canova, M., Cao, L.R., and Co, A.C. (2014). In situ quantification and visualization of lithium transport with neutrons. Angew. Chem. *126*, 9652–9656.

20. Ziesche, R.F., Kardjilov, N., Kockelmann, W., Brett, D.J., and Shearing, P.R. (2022). Neutron imaging of lithium batteries. Joule *6*, 35–52.

21. Han, F., Westover, A.S., Yue, J., Fan, X., Wang, F., Chi, M., Leonard, D.N., Dudney, N.J., Wang, H., and Wang, C. (2019). High electronic conductivity as the origin of lithium dendrite formation within solid electrolytes. Nat. Energy *4*, 187–196.

22. Liu, T., Leskes, M., Yu, W., Moore, A.J., Zhou, L., Bayley, P.M., Kim, G., and Grey, C.P. (2015). Cycling Li-O_2 batteries via LiOH formation and decomposition. Science *350*, 530–533.

23. Liu, H., Strobridge, F.C., Borkiewicz, O.J., Wiaderek, K.M., Chapman, K.W., Chupas, P.J., and Grey, C.P. (2014). Capturing metastable structures during high-rate cycling of $LiFePO_4$ nanoparticle electrodes. Science *344*, 1252817.

24. Pecher, O., Carretero-González, J., Griffith, K.J., and Grey, C.P. (2017). Materials' methods: NMR in battery research. Chem. Mater. *29*, 213–242.

25. Boyle, D.T., Huang, W., Wang, H., Li, Y., Chen, H., Yu, Z., Zhang, W., Bao, Z., and Cui, Y. (2021). Corrosion of lithium metal anodes during calendar ageing and its microscopic origins. Nat. Energy *6*, 487–494.

26. Bikondoa, O., and Carbone, D. (2021). On Compton scattering as a source of background in coherent diffraction imaging experiments. J. Synchrotron Radiat. *28*, 538–549.

27. Wang, D., Xiea, H., Liu, Q., Mu, K., Song, Z., Xu, W., Tian, L., Zhu, C., and Xu, J. (2023). Low-Cost, High-Strength Cellulose-based Quasi-Solid Polymer Electrolyte for Solid-State Lithium-Metal Batteries. Angew. Chem., Int. Ed. Engl. *62*, e202302767.

28. Huang, C., Leung, C.L.A., Leung, P., and Grant, P.S. (2021). A solid-state battery cathode with a polymer composite electrolyte and low tortuosity microstructure by directional freezing and polymerization. Adv. Energy Mater. *11*, 2002387.

29. Wu, J., Yuan, L., Zhang, W., Li, Z., Xie, X., and Huang, Y. (2021). Reducing the thickness of solid-state electrolyte membranes for high-energy lithium batteries. Energy Environ. Sci. *14*, 12–36.

30. Wang, H., Han, Y.-L., Su, F.-Y., Yi, Z.-L., Xie, L.-J., Sun, G.-H., Huang, X.-H., Chen, J.-P., Li, X.-M., Wang, Z.-B., and Chen, C.M. (2024). Internal pressure regulation enables reliable electrochemical performance evaluation of lithium-ion full coin cell. J. Power Sources *600*, 234235.

31. Leung, C.L.A., Wilson, M.D., Connolley, T., Collins, S.P., Magdysyuk, O.V., Boone, M.N., Suzuki, K., Veale, M.C., Liotti, E., Van Assche, F., et al. (2023). Correlative full field X-ray compton scattering imaging and X-ray computed tomography for in situ observation of Li ion batteries. Mater. Today Energy *31*, 101224.

32. Vo, N.T., Atwood, R.C., Drakopoulos, M., and Connolley, T. (2021). Data processing methods and data acquisition for samples larger than the field of view in parallel-beam tomography. Opt Express *29*, 17849–17874.

33. Huang, C., Wilson, M.D., Suzuki, K., Liotti, E., Connolley, T., Magdysyuk, O.V., Collins, S., Van Assche, F., Boone, M.N., Veale, M.C., et al. (2022). 3D Correlative Imaging of Lithium Ion Concentration in a Vertically Oriented Electrode Microstructure with a Density Gradient. Adv. Sci. *9*, 2105723.

34. Veale, M.C., Booker, P., Cross, S., Hart, M.D., Jowitt, L., Lipp, J., Schneider, A., Seller, P., Wheater, R.M., Wilson, M.D., et al. (2020). Characterization of the Uniformity of High-Flux CdZnTe Material. Sensors *20*, 2747.

35. Koch-Mehrin, K.A.L., Bugby, S.L., Lees, J.E., Veale, M.C., and Wilson, M.D. (2021). Charge sharing and charge loss in high-flux capable pixelated CdZnTe detectors. Sensors *21*, 3260.

36. Marker, K., Reeves, P.J., Xu, C., Griffith, K.J., and Grey, C.P. (2019). Evolution of structure and lithium dynamics in $LiNi_{0.8}Mn_{0.1}Co_{0.1}O_2$ (NMC811) cathodes during electrochemical cycling. Chem. Mater. *31*, 2545–2554.

37. Dudney, N.J., and Jang, Y.-I. (2003). Analysis of thin-film lithium batteries with cathodes of 50 nm to 4 μm thick $LiCoO_2$. J. Power Sources *119–121*, 300–304.

38. Jang, Y.-I., Neudecker, B.J., and Dudney, N.J. (2001). Lithium diffusion in Li_xCoO_2 (0.45< x< 0.7) intercalation cathodes. Electrochem. Solid State Lett. *4*, A74.

39. Barker, J., Pynenburg, R., Koksbang, R., and Saidi, M. (1996). An electrochemical investigation into the lithium insertion properties of Li_xCoO_2. Electrochim. Acta *41*, 2481–2488.

40. Huang, C., Dontigny, M., Zaghib, K., and Grant, P.S. (2019). Low-tortuosity and graded lithium ion battery cathodes by ice templating. J. Mater. Chem. A Mater. *7*, 21421–21431.

41. Sångeland, C., Hernández, G., Brandell, D., Younesi, R., Hahlin, M., and Mindemark, J. (2022). Dissecting the Solid Polymer Electrolyte–Electrode Interface in the Vicinity of Electrochemical Stability Limits. ACS Appl. Mater. Interfaces *14*, 28716–28728.

42. Weiss, M., Ruess, R., Kasnatscheew, J., Levartovsky, Y., Levy, N.R., Minnmann, P., Stolz, L., Waldmann, T., Wohlfahrt-Mehrens, M., Aurbach, D., et al. (2021). Fast charging of lithium-ion batteries: a review of materials aspects. Adv. Energy Mater. *11*, 2101126.

43. Nomura, Y., Yamamoto, K., Yamagishi, Y., and Igaki, E. (2021). Lithium transport pathways guided by grain architectures in Ni-rich layered cathodes. ACS Nano *15*, 19806–19814.

44. Balke, N., Jesse, S., Morozovska, A.N., Eliseev, E., Chung, D.W., Kim, Y., Adamczyk, L., García, R.E., Dudney, N., and Kalinin, S.V. (2010). Nanoscale mapping of ion diffusion in a lithium-ion battery cathode. Nat. Nanotechnol. *5*, 749–754.

45. Ruess, R., Schweidler, S., Hemmelmann, H., Conforto, G., Bielefeld, A., Weber, D.A., Sann, J., Elm, M.T., and Janek, J. (2020). Influence of NCM particle cracking on kinetics of lithium-ion batteries with liquid or solid electrolyte. J. Electrochem. Soc. *167*, 100532.

46. Dugas, R., Dupraz, Y., Quemin, E., Koç, T., and Tarascon, J.-M. (2021). Engineered three-electrode cells for improving solid state batteries. J. Electrochem. Soc. *168*, 090508.

47. Nam, Y.J., Park, K.H., Oh, D.Y., An, W.H., and Jung, Y.S. (2018). Diagnosis of failure modes for all-solid-state Li-ion batteries enabled by three-electrode cells. J. Mater. Chem. A Mater. *6*, 14867–14875.

48. Ikezawa, A., Fukunishi, G., Okajima, T., Kitamura, F., Suzuki, K., Hirayama, M., Kanno, R., and Arai, H. (2020). Performance of $Li_4Ti_5O_{12}$-based reference electrode for the electrochemical analysis of all-solid-state lithium-ion batteries. Electrochem. Commun. *116*, 106743.

49. Lu, J., Zhou, J., Chen, R., Fang, F., Nie, K., Qi, W., Zhang, J.-N., Yang, R., Yu, X., Li, H., et al. (2020). 4.2 V poly(ethylene oxide)-based all-solid-state lithium batteries with superior cycle and safety performance. Energy Storage Mater. *32*, 191–198.

50. Huang, C., Young, N.P., Zhang, J., Snaith, H.J., and Grant, P.S. (2017). A two layer electrode structure for improved Li ion diffusion and volumetric capacity in Li ion batteries. Nano Energy *31*, 377–385.

51. Huang, C., Young, N.P., and Grant, P.S. (2014). Spray processing of TiO_2 nanoparticle/ionomer coatings on carbon nanotube

scaffolds for solid-state supercapacitors. J. Mater. Chem. A Mater. *2*, 11022–11028.

52. Qiu, J., Liu, X., Chen, R., Li, Q., Wang, Y., Chen, P., Gan, L., Lee, S.J., Nordlund, D., Liu, Y., et al. (2020). Enabling stable cycling of 4.2 V high-voltage all-solid-state batteries with PEO-based solid electrolyte. Adv. Funct. Mater. *30*, 1909392.

53. Li, J., Li, F., Zhang, L., Zhang, H., Lassi, U., and Ji, X. (2021). Recent applications of ionic liquids in quasi-solid-state lithium metal batteries. Green Chemical Engineering *2*, 253–265.

54. Kim, J.-S., Yoon, G., Kim, S., Sugata, S., Yashiro, N., Suzuki, S., Lee, M.-J., Kim, R., Badding, M., Song, Z., et al. (2023). Surface engineering of inorganic solid-state electrolytes via interlayers strategy for developing long-cycling quasi-all-solid-state lithium batteries. Nat. Commun. *14*, 782.

55. Van Assche, F., Vanheule, S., Van Hoorebeke, L., and Boone, M.N. (2021). The spectral x-ray imaging data acquisition (spexidaq) framework. Sensors *21*, 563.

56. Suzuki, K., Barbiellini, B., Orikasa, Y., Kaprzyk, S., Itou, M., Yamamoto, K., Wang, Y.J., Hafiz, H., Uchimoto, Y., Bansil, A., et al. (2016). Non-destructive measurement of in-operando lithium concentration in batteries via x-ray Compton scattering. J. Appl. Phys. *119*, 025103.

57. Cooper, M., Cooper, M.J., Mijnarends, P., Mijnarends, P.E., Shiotani, N., Sakai, N., and Bansil, A. (2004). X-Ray Compton Scattering (Oxford University Press on Demand).

58. Stephanos, J.J., and Addison, A.W. (2017). Electrons, Atoms, and Molecules in Inorganic Chemistry: A Worked Examples Approach (Academic Press).

59. Brancewicz, M., Itou, M., and Sakurai, Y. (2016). A Monte Carlo study of high-energy photon transport in matter: application for multiple scattering investigation in Compton spectroscopy. J. Synchrotron Radiat. *23*, 244–252.

60. Bugby, S., Koch-Mehrin, K., Veale, M., Wilson, M., and Lees, J. (2019). Energy-loss correction in charge sharing events for improved performance of pixellated compound semiconductors. Nucl. Instrum. Methods Phys. Res. Sect. A Accel. Spectrom. Detect. Assoc. Equip. *940*, 142–151.

61. Wan, J., Xie, J., Kong, X., Liu, Z., Liu, K., Shi, F., Pei, A., Chen, H., Chen, W., Chen, J., et al. (2019). Ultrathin, flexible, solid polymer composite electrolyte enabled with aligned nanoporous host for lithium batteries. Nat. Nanotechnol. *14*, 705–711.

62. Friedrich, F., Strehle, B., Freiberg, A.T.S., Kleiner, K., Day, S.J., Erk, C., Piana, M., and Gasteiger, H.A. (2019). Capacity fading mechanisms of NCM-811 cathodes in lithium-ion batteries studied by X-ray diffraction and other diagnostics. J. Electrochem. Soc. *166*, A3760–A3774.

63. Vamvakeros, A., Matras, D., Ashton, T.E., Coelho, A.A., Dong, H., Bauer, D., Odarchenko, Y., Price, S.W.T., Butler, K.T., Gutowski, O., et al. (2021). Cycling Rate-Induced Spatially-Resolved Heterogeneities in Commercial Cylindrical Li-Ion Batteries. Small Methods *5*, 2100512.

64. Egami, T., and Billinge, S.J. (2003). Underneath the Bragg Peaks: Structural Analysis of Complex Materials*16* (Elsevier).

65. Itou, M., Orikasa, Y., Gogyo, Y., Suzuki, K., Sakurai, H., Uchimoto, Y., and Sakurai, Y. (2015). Compton scattering imaging of a working battery using synchrotron high-energy X-rays. J. Synchrotron Radiat. *22*, 161–164.

66. Suzuki, K., Kanai, R., Tsuji, N., Yamashige, H., Orikasa, Y., Uchimoto, Y., Sakurai, Y., and Sakurai, H. (2018). Dependency of the Charge–Discharge Rate on Lithium Reaction Distributions for a Commercial Lithium Coin Cell Visualized by Compton Scattering Imaging. Condensed Matter *3*, 27.

67. Wang, C., Wang, X., Zhang, R., Lei, T., Kisslinger, K., and Xin, H.L. (2023). Resolving complex intralayer transition motifs in high-Ni-content layered cathode materials for lithium-ion batteries. Nat. Mater. *22*, 235–241.

68. Yang, H., and Wu, N. (2022). Ionic conductivity and ion transport mechanisms of solid-state lithium-ion battery electrolytes: A review. Energy Sci. Eng. *10*, 1643–1671.

69. Adenusi, H., Chass, G.A., Passerini, S., Tian, K.V., and Chen, G. (2023). Lithium batteries and the solid electrolyte interphase (SEI)—Progress and outlook. Adv. Energy Mater. *13*, 2203307.

70. Li, J., Dudney, N.J., Xiao, X., Cheng, Y.T., Liang, C., and Verbrugge, M.W. (2015). Asymmetric rate behavior of Si anodes for lithium-ion batteries: ultrafast de-lithiation versus sluggish lithiation at high current densities. Adv. Energy Mater. *5*, 1401627.

71. Mirsakiyeva, A., Ebadi, M., Araujo, C.M., Brandell, D., Broqvist, P., and Kullgren, J. (2019). Initial steps in PEO decomposition on a Li metal electrode. J. Phys. Chem. C *123*, 22851–22857.

72. Hu, J., Wu, B., Chae, S., Lochala, J., Bi, Y., and Xiao, J. (2021). Achieving highly reproducible results in graphite-based Li-ion full coin cells. Joule *5*, 1011–1015.

73. Sedlatschek, T., Lian, J., Li, W., Jiang, M., Wierzbicki, T., Bazant, M.Z., and Zhu, J. (2021). Large-deformation plasticity and fracture behavior of pure lithium under various stress states. Acta Mater. *208*, 116730.

74. Pei, A., Zheng, G., Shi, F., Li, Y., and Cui, Y. (2017). Nanoscale nucleation and growth of electrodeposited lithium metal. Nano Lett. *17*, 1132–1139.

75. Khurana, R., Schaefer, J.L., Archer, L.A., and Coates, G.W. (2014). Suppression of lithium dendrite growth using cross-linked polyethylene/poly (ethylene oxide) electrolytes: a new approach for practical lithium-metal polymer batteries. J. Am. Chem. Soc. *136*, 7395–7402.

76. Huang, C., and Grant, P.S. (2018). Coral-like directional porosity lithium ion battery cathodes by ice templating. J. Mater. Chem. A Mater. *6*, 14689–14699.

77. Kasemchainan, J., Zekoll, S., Spencer Jolly, D., Ning, Z., Hartley, G.O., Marrow, J., and Bruce, P.G. (2019). Critical stripping current leads to dendrite formation on plating in lithium anode solid electrolyte cells. Nat. Mater. *18*, 1105–1111.

78. Louli, A.J., Coon, M., Genovese, M., Degooyer, J., Eldesoky, A., and Dahn, J.R. (2021). Optimizing cycling conditions for anode-free lithium metal cells. J. Electrochem. Soc. *168*, 020515.

79. Xiong, Z., Wang, Z., Zhou, W., Liu, Q., Wu, J.-F., Liu, T.-H., Xu, C., and Liu, J. (2023). 4.2 V polymer all-solid-state lithium batteries enabled by high-concentration PEO solid electrolytes. Energy Storage Mater. *57*, 171–179.